ACS Energy LETTERS

http://pubs.acs.org/journal/aelccp

Suppressed Proton Insertion Enhances Zinc-Ion Storage Kinetics and Stability in Hydrated Vanadate

Published as part of ACS Energy Letters special issue "The Evolving Landscape of Energy Research: Insights from Leading Researchers".

Heng Liu, Menghao Yang, Quan Zong, Min-Hsin Yeh, Chun-Chi Chang, Long Yang, Wei-Hsiang Huang,* Chaofeng Liu,* and Guozhong Cao*

Cite This: https://doi.org/10.1021/acsenergylett.5c03338

ABSTRACT: Preintercalation chemistry is pivotal for tuning the structure of layered hydrated vanadium pentoxide (V_2O_5·nH_2O, VOH) cathodes in aqueous zinc-ion batteries (AZIBs). However, the underlying fundamental impacts on proton insertion accompanied by zinc storage are elusive in the electrochemical process. In this work, 1,3-diaminoguanidine (DG) molecules are preintercalated into the interlayers of VOH. The modified sample (DG-VOH) exhibits enhanced Zn^{2+} diffusion and storage despite the reduced interlayer spacing. This improvement stems from the charge shielding effect provided by preintercalated DG molecules. Additionally, distortion of [VO_6] octahedra modulates the electronic structure, leading to increased electronic conductivity. More importantly, the modulated electronic structure contributes to the effectively suppressed detrimental H^+ co-insertion, which alleviates lattice strain, vanadium dissolution, and byproduct formation. As a result, the DG-VOH cathode delivers a high specific capacity of 437.8 mAh/g and outstanding long-term cycling stability, retaining 91% of its capacity after 5000 cycles at 8 A/g. This work elucidates the critical role of organic preintercalants in inhibiting H^+ co-intercalation, providing valuable insights for the design of high-performance AZIB cathodes.

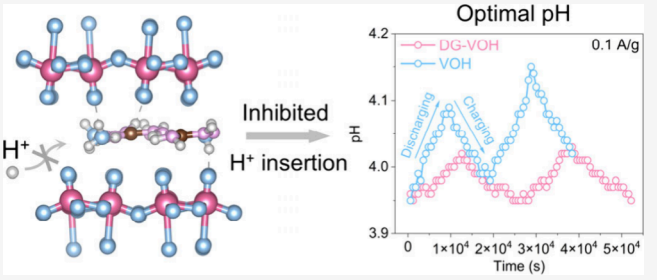

The challenges posed by fossil fuel consumption and environmental pollution are becoming increasingly critical. This urgency has expedited the utilization of green and renewable energy resources, such as solar and wind power, which depend on large-scale energy storage devices to overcome their geographic limitations and intermittency. Lithium-ion batteries (LIBs), as a representative of electrochemical energy storage, are prevailing in smart electronics and electric vehicles due to their high energy density, fast response, and flexible configuration.[1] However, the high-cost, flammability, and environmental concerns hinder their further deployment in large-scale energy storage.[2] Aqueous zinc-ion batteries (AZIBs) based on a nonflammable aqueous electrolyte and low-cost zinc metal anode, offer advantages of economic viability, high safety, and environmental friendliness, rendering them promising candidates for large-scale energy storage.[3−6] Nevertheless, the advancement of AZIBs is still mainly impeded by cathode materials that deliver relatively low capacity and limited cycle stability, underscoring the urgent need for the exploration of optimized cathode materials.

The layered structure of hydrated vanadium pentoxide (V_2O_5·nH_2O) exhibits significant structural versatility, enabling the preintercalation of a wide variety of guest species.[7−9] In particular, its interlayer space can be tailored through accommodating a wide array of ions and molecules, ranging from metal cations (Li^+, Ca^{2+}, Ni^{2+}, etc.) and water molecules to more complex organic species (ethylene glycol, $C_{10}H_{16}N^+$, polyaniline, etc.).[10−15] Extensive studies have greatly advanced the understanding of preintercalation chemistry. Early studies

Received: October 14, 2025
Revised: December 7, 2025
Accepted: December 10, 2025

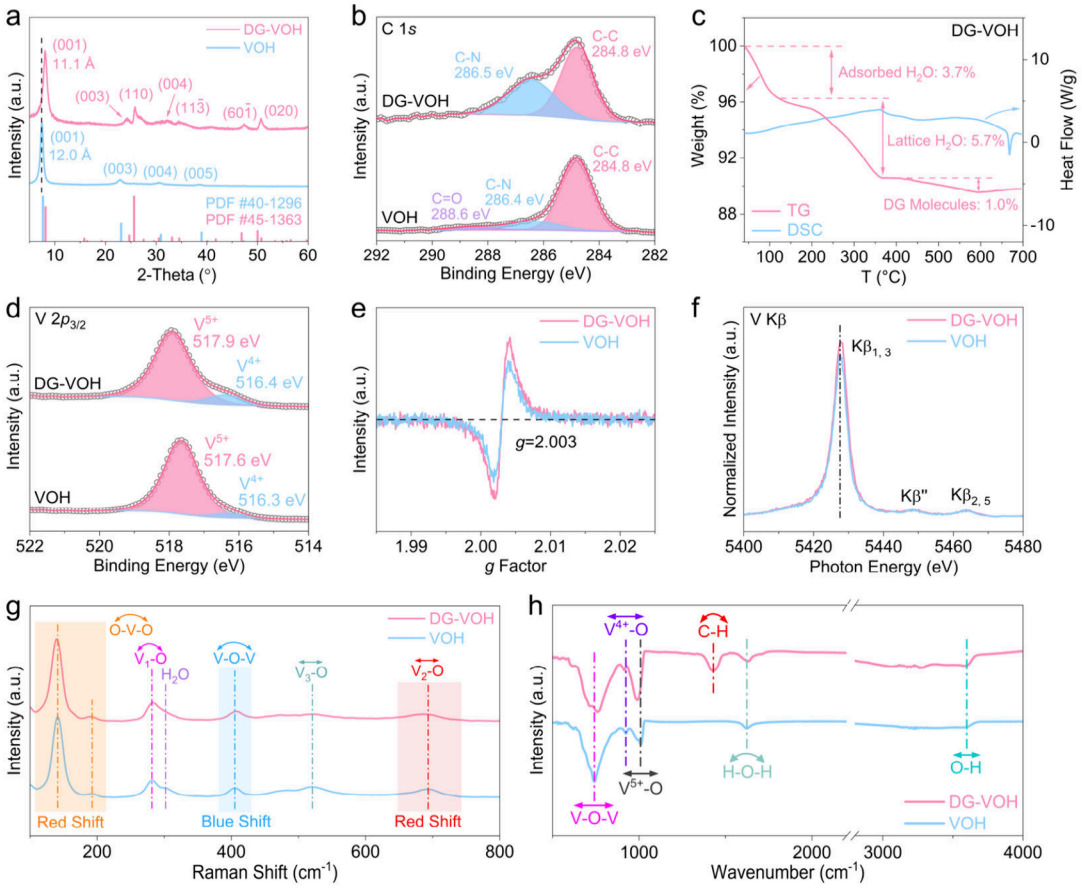

Figure 1. Structures and chemical states of DG-VOH and VOH. (a) XRD patterns. (b) XPS spectra of C 1*s*. (c) TG-DSC curves of the DG-VOH. (d) XPS spectra of V $2p_{3/2}$. (e) EPR spectra. (f) XES spectra of the V K*β*-edge. (g) Raman spectra. (h) FTIR spectra.

primarily emphasized enlarging the interlayer spacing to improve kinetics and reinforcing the lattice to enhance cycling stability.[12,16,17] For instance, the preintercalation of ethylenediamine (EDA) molecules both supported the [VO] layers and expanded the interlayer spacing of (002) to 9.61 Å. The resulting cathode delivered a significantly improved specific capacity of 382.6 mAh/g at 0.5 A/g and exhibited an ultralow capacity fading rate of 0.047‰ per cycle at 5 A/g.[18] More recently, research efforts have shifted toward thermodynamic optimization strategies aimed at widening the working voltage window and increasing the midpoint voltage.[14,19,20] For example, the preintercalation of benzyltrimethylammonium cations expanded the voltage window of VOH from the conventional 0.2−1.6 V to 0.2−1.8 V without sacrificing cycling stability, enabling a ∼15% enhancement in energy density at the material level.[14] In addition, preintercalating chlorcholine cations into VOH increased the working midpoint voltage by ∼50 mV, which is a 10% increase compared with the pristine sample.[20] Despite these advances, critical challenges still remain in deciphering the fundamental influence of intercalants on the $V_2O_5{\cdot}nH_2O$ host lattice, particularly with respect to the band structure modulation and electrode−electrolyte interface. This knowledge gap in the structure−function relationship continues to restrict the systematic enhancement of these cathode materials for ZIBs, necessitating a comprehensive mechanistic understanding of guest species preintercalation.

This study investigates 1,3-diaminoguanidine (DG) molecules preintercalated hydrated vanadium pentoxide (DG-VOH) as a cathode material for aqueous zinc-ion batteries. Unlike common conventional strategies that expand interlayer spacing, DG preintercalation results in lattice contraction while simultaneously enhancing Zn^{2+} diffusion through a charge shielding effect. In addition, the intercalated DG molecules induce local distortion in the [VO_6] octahedra, which improve electronic conductivity via reducing the energies of V 3*d* and O 2*p* bands, making the Fermi level across the conduction band. Moreover, the downshifted V 3*d* states in DG-VOH weaken proton (H^+) adsorption, effectively suppressing detrimental H^+ co-insertion to prevent the structural collapse, hinder by-product formation, and suppress vanadium dissolution, ensuring structural integrity. As a result, the DG-VOH cathode delivers a high capacity of 437.8 mAh/g and remarkable cycling stability (91% retention after 5000 cycles), offering a general design strategy for high-performance cathode materials.

Figure 1a shows the XRD patterns of both samples. The diffraction peaks of VOH match well with the polycrystalline $V_2O_5{\cdot}1.6H_2O$ phase (JCPDS NO. 40-1296), which has a bilayered structure, and the lattice water molecules are accommodated between [VO] layers. The (001) peak at 7.4° corresponds to an interplanar spacing of 12.0 Å. By contrast, the pattern of DG-VOH is consistent with the (Na, Ca)(V, Fe)$_8O_{20}{\cdot}nH_2O$ phase (JCPDS No. 45-1363), which has the same bilayered structure as $V_2O_5{\cdot}1.6H_2O$ phase but displays additional peaks originating from the changed local symmetry.[21] For DG-VOH, the interplanar spacing of (001) shrinks to 11.1 Å compared to that of 12.0 Å for VOH, suggesting the narrowed [VO] interlayer spacing after the preintercalation of

https://doi.org/10.1021/acsenergylett.5c03338
ACS Energy Lett. XXXX, XXX, XXX−XXX

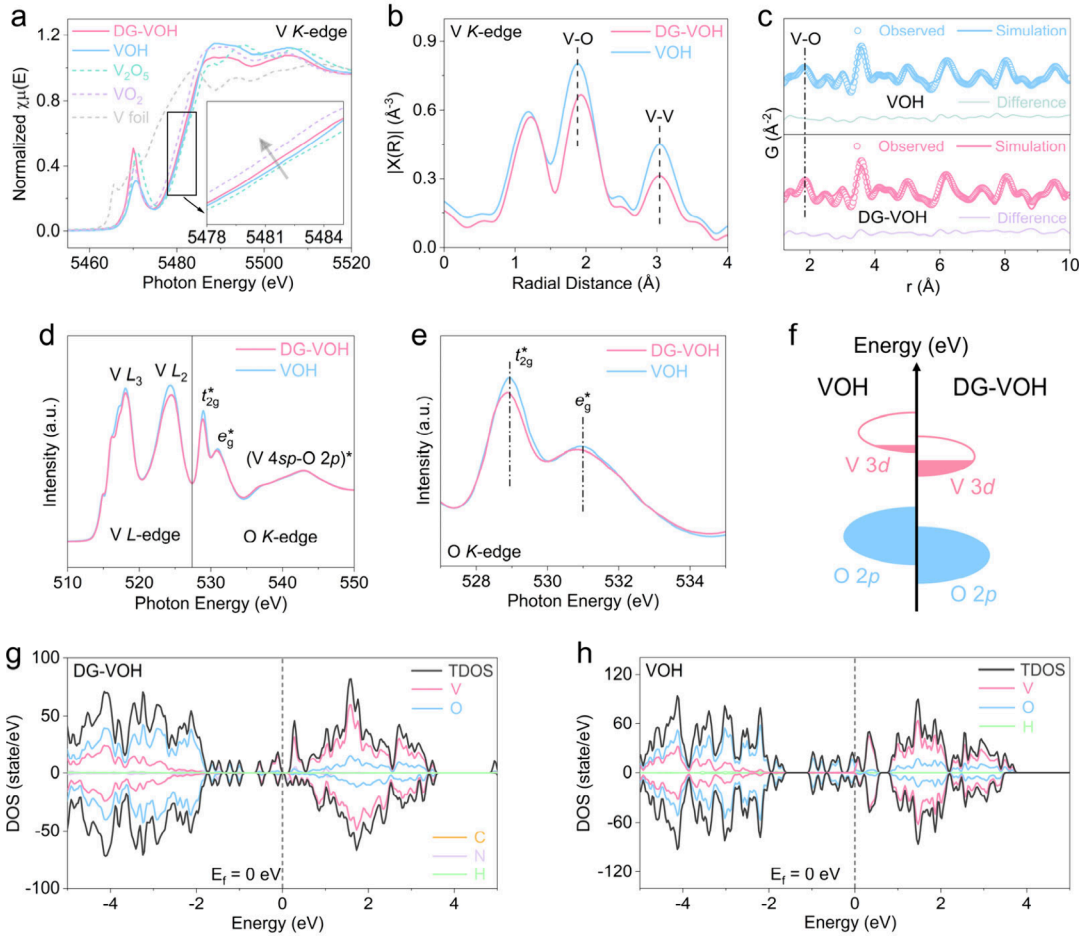

Figure 2. Local structure and orbital energy levels. (a) V *K*-edge XANES spectra of DG-VOH, VOH, and reference samples (V_2O_5, VO_2, and V foil). (b) k^2-weighted Fourier transform of the V *K*-edge EXAFS. (c) X-ray pair distribution function (PDF) data and PDF refinement results of both samples. (d) V *L*-edge and O *K*-edge XANES spectra of DG-VOH and VOH. (e) *K*-edge XANES spectra of both samples. (f) Schematic illustration of the energy diagram of both samples. Density of states (DOS) of (g) DG-VOH and (h) VOH.

DG molecules. High-resolution transmission electron microscopy (HRTEM) images of DG-VOH in Figure S1 further verify the narrowed (001) interlayer spacing, which can be attributed to the polar DG molecules developing strong electrostatic interaction with [VO] layers and drawing layers closer to each other in comparison with lattice water. The TEM-EDS elemental mappings of DG-VOH (Figure S2) also confirm the homogeneous distribution of V, O, C, and N elements in DG-VOH. Figure 1b presents the XPS C 1*s* spectra of both samples. For VOH, the C−C, C=O, and C−N signals originate from the adventitious carbon/nitrogen contamination.[22] In contrast, DG-VOH exhibits a much stronger C−N signal than VOH, demonstrating its incorporation of nitrogen-containing organic species, mainly DG molecules. Thermogravimetric analysis-differential scanning calorimetry (TG-DSC) curves (Figure 1c and Figure S3) reveal that the lattice water content in DG-VOH (5.7%) is lower than that in VOH (8.6%). The mass ratio of DG molecules is ∼1.0%, suggesting that preintercalation involves a relatively small amount of DG molecules. Due to the low content of intercalated DG molecules, the volume of lost lattice water between [VO] layers in DG-VOH is not fully compensated, leading to the shrinkage of interlayer spacing verified by XRD patterns. The XPS spectra of V $2p_{3/2}$ (Figure 1d) show peaks corresponding to V^{5+} (higher binding energy) and V^{4+} (lower binding energy).[19] DG-VOH has a higher V^{4+} peak intensity than VOH, indicating the higher mixed valence state of vanadium in DG-VOH. This finding is consistent with the enhanced EPR signal intensity of DG-VOH in Figure 1e. This reduction of vanadium is usually ascribed to the formation of oxygen vacancies during hydro-thermal synthesis, which is accompanied by the partial oxidation of DG molecules.[13] The O 1*s* spectra in Figure S4 reveal that the peak of oxygen vacancies (O_d) is located at 531.6 eV for DG-VOH and 531.4 eV for VOH. The ratio of the O_d peak is 14.5% for DG-VOH, and it is 11.9% for VOH, indicating the higher concentration of oxygen vacancies in DG-VOH. Thus, vanadium in DG-VOH is reduced to balance the charge of formed oxygen vacancies. The higher content of unpaired electrons of V^{4+} in DG-VOH benefits its electronic conductivity.[16] Figure 1f shows the V Kβ-edge X-ray emission spectra (XES). The K$\beta_{1,3}$ peak, originating from V 3*p* to V 1*s* transition and sensitive to the local electronic environment of vanadium,[23] shifts to higher energy by ∼0.3 eV compared with that of VOH, further confirming DG-VOH has a higher mixed valence states of vanadium. The Kβ'' and K$\beta_{2,5}$ peaks, corresponding to the valence-to-core electronic transition from the O 2s orbital to the β 1s orbital, exhibit negligible differences between the two samples. Figure 1g shows the Raman spectra of both samples. The characteristic peaks at

https://doi.org/10.1021/acsenergylett.5c03338
ACS Energy Lett. XXXX, XXX, XXX−XXX

Table 1. PDF Structural Refinement Results for DG-VOH and VOH over the Range of 1.2 < r < 11.5 Å[a]

VOH				DG-VOH			
Lattice parameter: a = 11.8740 Å, b = 3.5900 Å, c = 11.6276 Å, β = 88.65°				Lattice parameter: a = 11.8453 Å, b = 3.6183 Å, c = 11.4046 Å, β = 88.65°			
Atom	x	z	U_{iso} [Å^2]	Atom	x	z	U_{iso} [Å^2]
V (1)	0.9307	0.1295	0.0037	V (1)	0.9317	0.1301	0.0057
V (2)	0.2246	0.1321	0.0037	V (2)	0.2255	0.1335	0.0057
O (1)	0.3911	0.1063	0.0168	O (1)	0.3939	0.1074	0.0019
O (2)	0.0856	0.0839	0.0168	O (2)	0.0786	0.0875	0.0019
O (3)	0.7442	0.0768	0.0168	O (3)	0.7491	0.0670	0.0019
O (4)	0.9339	0.2813	0.0168	O (4)	0.9085	0.2750	0.0019
O (5)	0.1945	0.2625	0.0168	O (5)	0.2009	0.2629	0.0019
O*	0.5737	0.4903	0.1044	O*	0.4448	0.4997	0.1723

[a]Here, x and z are the refinable atomic positions in the fractional coordinate of the V and O sites. U_{iso}, in units of Å^2, is the isotropic atomic displacement parameter (ADP). O* represents the oxygen of lattice water.

141.0 and 192.7 cm^{-1} are attributed to the bending vibration of O−V−O bonds, and the peak at 405.3 cm^{-1} originats from V−O−V bending vibration.[19,24] These two bending vibration modes reveal the vibrations of the [VO] framework. Compared with VOH, the red shift of the O−V−O bonds and the blue shift of the V−O−V bonds in DG-VOH indicate that some V−O bonds are elongated and the others are shortened after DG preintercalation, indicative of lattice distortion. The peaks at 281.6, 520.6, and 693.5 cm^{-1} correspond to the bending/stretching vibration modes of V_x−O bonds, where x means the oxygen atom is shared by x vanadium atoms.[25] The shifts of these peaks are a result of the presence of lattice distortion. Fourier transform infrared (FTIR) spectra of DG-VOH in Figure 1h show a notable peak at ∼1431.1 cm^{-1}, which is caused by the bending vibration of C−H bonds in DG molecules, further verifying the preintercalation of DG molecules. The characteristic peak at 741.0 cm^{-1} originates from the stretching vibration of V−O−V bonds.[26] The splitting of this peak in DG-VOH also suggests the anisotropic distortion of the [VO] framework. The red shifts of V^{4+}−O (925.3 cm^{-1}) and V^{5+}−O (1008.0 cm^{-1}) modes indicate elongation of average V−O bond lengths compared with that of VOH.[25]

Figure 2a shows the experimental V K-edge X-ray absorption near-edge structure (XANES) spectra of DG-VOH, VOH, V_2O_5, VO_2 and V foil. DG-VOH has lower absorption edge energy and pre-edge peak energy than those of VOH, further verifying its lower valence of vanadium.[14] The absorption edge of DG-VOH and VOH both lie between those of VO_2 and V_2O_5, suggesting the valence of vanadium in both samples is between 4+ and 5+. The higher pre-edge peak intensity of DG-VOH suggests a reduced local symmetry and higher distorted [VO_6] octahedra.[8] To deeply investigate the local distortion, the k^2-weighted Fourier transform of the extended X-ray absorption fine structure (EXAFS) in Figure 2b is analyzed. The peaks at ∼1.9 Å correspond to the V−O bonds within the [VO_6] octahedra (the first coordination sphere). The radial distance of this peak reflects the average V−O bond length, and its intensity relates to the coordination number of vanadium.[27] Compared with VOH, the right shift of the V−O peak in DG-VOH by ∼0.05 Å indicates its larger average V−O bond length, which is in accordance with the FTIR results. The lower V−O peak intensity suggests a reduced vanadium coordination number in DG-VOH, further confirming the formation of oxygen vacancies. The local structure information was also investigated using X-ray pair distribution function (PDF) analysis (Figure 2c).[28,29] The peaks at ∼1.9 Å correspond to the average V−O bond length in the first coordination shell.[30] For DG-VOH, this peak shifts to slightly higher r compared with that of VOH, suggesting that the V−O bonds in DG-VOH are longer than those of VOH on average, substantiating the EXAFS findings. The increased average V−O bond length in DG-VOH is due to its higher content of V^{4+}, which has a larger ionic radius than V^{5+}.[16] The refined structural information is listed in Table 1, and the crystallographic model used for refinement is shown in Figure S5. V(x)/O(y) stands for vanadium/oxygen atom with different coordination environments. Visualization of the refined atomic positions using VESTA reveals that in DG-VOH, the V1−O1, V2−O1, V2−O2, and V2−O3 bonds are elongated, and the V1−O2, V1−O3, V1−O4, and V2−O5 bonds are shortened compared with in VOH. These changes agree well with Raman spectra. The partial PDF curves of DG-VOH and VOH in Figure S6 support the contribution of each atomic pair to the total PDF in both samples. DG-VOH and VOH show similar partial and total PDF patterns. For the total PDF of both samples (Figure 2c), the greatest part of the peak at ∼1.8 Å is attributed to the V−O atomic pair within the first coordination shell of vanadium. The V−O pair at 1.89 Å in DG-VOH (Figure S6a) is longer than the 1.86 Å of VOH (Figure S6b), further verifying the average longer V−O bond length in DG-VOH. The peaks at ∼2.5 and 3.0 Å are contributed by the O−O and V−V atomic pair, respectively. The high peak at ∼3.6 Å is contributed by V−V pair. V−O and O−O pairs account for only a small extent of this peak. The peaks at the radial distance larger than 4 Å originate from the superposition of the V−O, O−O, and V−V pair distance beyond the first coordination shell. Figure 2d shows the V L-edge and O K-edge XANES spectra of DG-VOH and VOH. The V L-edge splits into V L_3-edge and V L_2-edge, which correspond to electron transition from V $2p_{3/2}$ to V $3d$ and V $2p_{1/2}$ to V $3d$, respectively.[31] Compared with VOH, the reduced peak intensities of V L_3-edge and V L_2-edge in DG-VOH indicate the higher electronic occupation of V $3d$ orbitals, which relates to the reduction of V^{5+}.[32] The O K-edge spectra correspond to electron transition from O $1s$ to unoccupied O $2p$ character orbitals in the conduction band,[31] namely, t_{2g}* antibonding orbitals, e_g* antibonding orbitals, and V $4sp$ - O $2p$ antibonding orbitals in both samples.[33] Among these three groups of antibonding orbitals, the t_{2g}* orbitals lie at the lowest energy level and are most likely to be occupied, followed by e_g* orbitals. The (V $4sp$ − O $2p$)* orbitals have the highest energy

https://doi.org/10.1021/acsenergylett.5c03338
ACS Energy Lett. XXXX, XXX, XXX−XXX

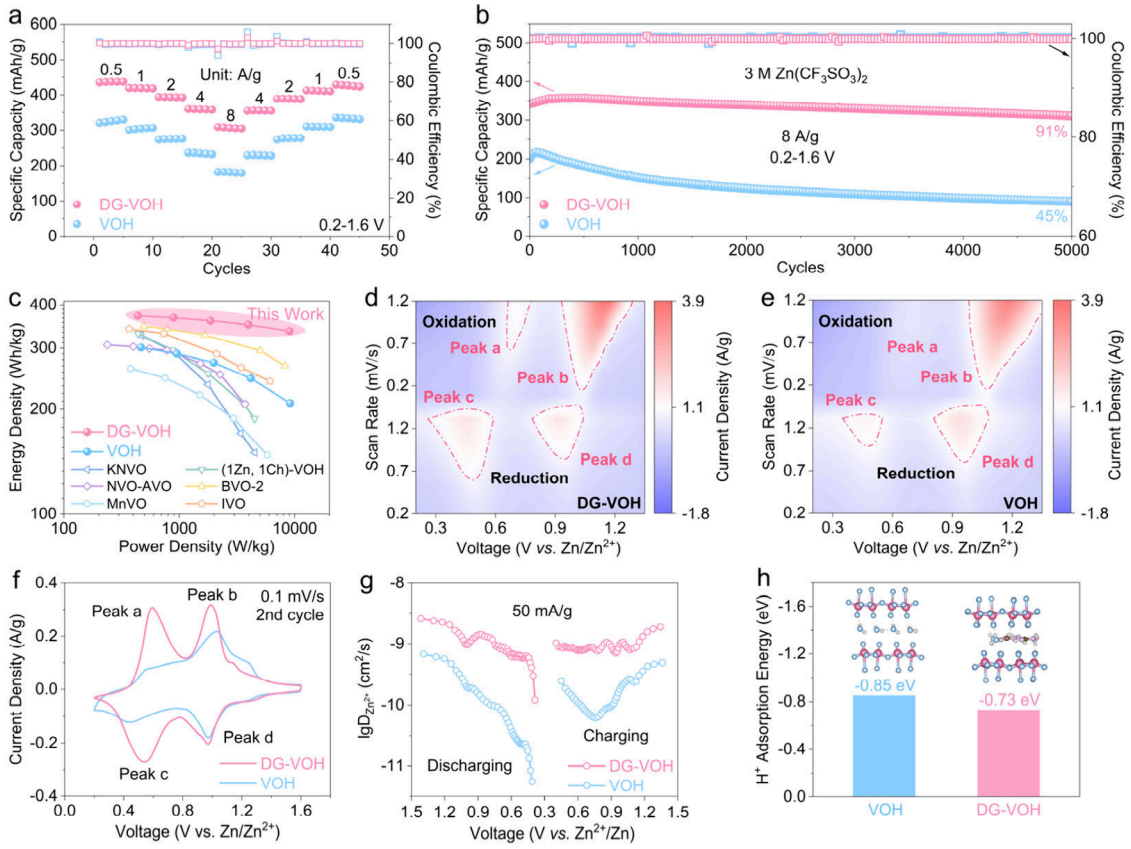

Figure 3. (a) Rate performance of both samples from 0.5 to 8 A/g. (b) Cycling performance at 8 A/g. (c) Ragone plots of DG-VOH, VOH, and some previously reported vanadium-based cathode materials. CV contours of (d) DG-VOH and (e) VOH from 0.2 to 1.2 mV/s. (f) CV curves of both samples at 0.1 mV/s. (g) $D_{Zn^{2+}}$ calculated according to the GITT curves. (h) H^+ adsorption energy of DG-VOH and VOH.

and are minimally occupied. Consequently, it is harder for O 1*s* electrons to transition to the higher occupied orbitals, resulting in lower transition intensity.[31] As shown in Figure 2e, DG-VOH displays a pronounced decrease of t_{2g}* peak compared with VOH, while the e_g* peak shows a slight reduction and the (V 4*sp* − O 2*p*)* peak remains nearly unchanged. The electronic structure of V^{5+} is $[Ar]3d^0$ and it is $[Ar]3d^1$ for V^{4+}. The higher V^{4+} ratio in DG-VOH leads to its higher V 3*d* occupancy, and the t_{2g}* orbitals are the lowest unoccupied orbitals for both samples. Therefore, the t_{2g}* occupancy of DG-VOH is higher than that of VOH, resulting in the significantly decreased t_{2g}* peak intensity.[31] As mentioned above, the conduction bands of both samples are determined by t_{2g}* and e_g* antibonding orbitals, which are dominated by V 3*d* orbitals.[33] Thus, many previous studies have named this band as the V 3*d* band, and so does this study. Notably, the t_{2g}* and e_g* peaks of DG-VOH both shift to lower energy relative to those of VOH, indicating a decreased energy level of the V 3*d* band. For the top of the valence band with a great proportion of O 2*p* character, we named it as O 2*p* band. The valence band region of XPS spectra for DG-VOH and VOH is shown in Figure S7. The left shift of DG-VOH suggests its reduced energy level of the O 2*p* band.[34] Based on the above discussion about the energy level of V 3*d* and O 2*p* bands, the band structure of both samples is illustrated in Figure 2f. Relative to VOH, DG-VOH has a higher V 3*d* band occupancy and shows lower energy levels of the V 3*d* and the O 2*p* bands. The density of states (DOS) calculation results of DG-VOH and VOH in Figure 2g,h further demonstrate their band structures. As illustrated, for both samples, the valence band majorly consists of O 2*p* orbitals, and the conduction band mainly consists of V 3*d* orbitals. For VOH, the bottom of the conduction band and the top of the valence band both approach the Fermi level. While for DG-VOH, the Fermi level crosses the conduction band and the top of valence band shifts left to about −1 eV, verifying its lower energy level of V 3*d* and O 2*p* bands and implying its improved electronic conductivity compared to that of VOH. Moreover, according to the d-band center theory,[35,36] the lower V 3*d* band of DG-VOH can reduce the adsorption of H_2O/H^+ on its lattice, suppressing detrimental side-reactions caused by active water molecules or hydrogen ions, which will be elaborated later.

Figure 3a shows the rate performance of DG-VOH and VOH. Within the current density ranges from 0.5 to 8 A/g, DG-VOH delivers markedly higher specific capacities than VOH, indicating its enhanced electrochemical kinetics due to the preintercalation of DG molecules. The specific capacity of DG-VOH decreases from 437.8 to 304.8 mAh/g as the current density increased from 0.5 to 8 A/g, corresponding to a retention of 69.6%. In contrast, VOH retains only 54.1% of its initial capacity under the same conditions, highlighting the superior rate performance of DG-VOH. The improved rate performance can be attributed to the optimized band structure, which accelerates electron transport and transfer processes. Electrochemical impedance spectroscopy (EIS) results in Figure S8 further support this argument. The semicircle in the high-frequency region and the oblique tail in the low-frequency region are attributed to the charge transfer resistance (R_{ct}) and Warburg resistance (W_o), respectively.[37] The reduced radius of the semicircle indicates the lower R_{ct} in

https://doi.org/10.1021/acsenergylett.5c03338
ACS Energy Lett. XXXX, XXX, XXX−XXX

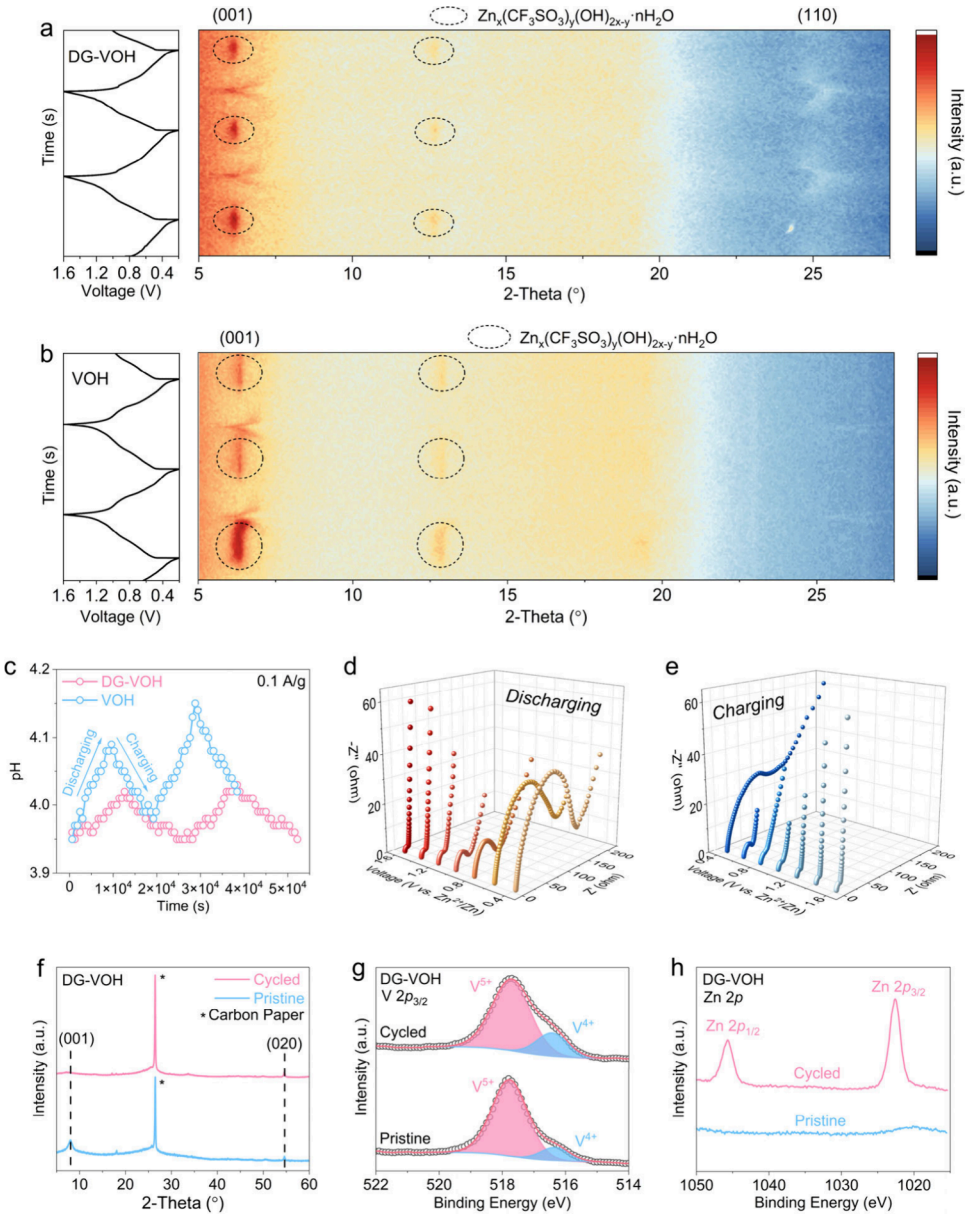

Figure 4. Charge storage mechanism of DG-VOH and VOH. In situ XRD patterns of (a) DG-VOH and (b) VOH for the initial three cycles. (c) *In situ* pH tests of both samples for the initial two cycles at 0.1 A/g. *In situ* EIS spectra of DG-VOH during (d) discharging and (e) charging process. (f) The XRD patterns of the postcycling (for 1000 cycles at 4 A/g) and the pristine states of DG-VOH cathode. The XPS spectra of (g) V $2p_{3/2}$ and (h) Zn 2*p* of the postcycling and the pristine states of DG-VOH cathode.

DG-VOH, further verifying its faster electron transport and transfer. Additionally, the preintercalated organic molecules can shield the positive charge of Zn^{2+} during charging and discharging, which reduces the binding interaction between lattice oxygen and zinc ions, leading to faster Zn^{2+} diffusion within the lattice.[38] Figure S9 shows the voltage profiles of both samples. The highly overlapped curves of DG-VOH indicate its excellent interfacial and structural stability. Figure 3b shows the cycling test of both samples at a rate of 8 A/g. DG-VOH has an initial specific capacity of 344.7 mAh/g and slightly increases to 358.1 mAh/g due to electrochemical activation. Then the specific capacity stays stable. After 5000 cycles, the specific capacity remains 91% of the initial (312.1 mAh/g), while VOH suffers significant capacity fading, which remains only 45% of the initial capacity. This contrast indicates the improved long-term cycling stability of DG-VOH. Figure 3c shows the Ragone plots of DG-VOH and VOH. At the material level, DG-VOH delivers an energy density of 372.4 Wh/kg at 439.7 W/kg and 336.6 Wh/kg at 9043.7 W/kg, outperforming VOH (301.4 Wh/kg at 466.0 W/kg and 208.6 Wh/kg at 9109.5 W/kg) and most previously reported vanadium-based cathodes.[16,39−43] Figure 3d,e presents the CV contours of DG-VOH and VOH, collected at the scan rate ranges from 0.2 to 1.2 mV/s. Peak a corresponds to the oxidation of V^{3+} to V^{4+}, and peak b relates to the oxidation of V^{4+} to V^{5+}. Peaks c and d are attributed to the reduction of V^{4+} to V^{3+} and the reduction of V^{5+} to V^{4+}, respectively.[25] DG-VOH shows higher intensities of peaks a and c, indicating its deeper utilization of the redox reaction of V^{4+}, which contributes to the enhanced specific capacity. Figure 3f shows the CV curves of both samples collected at a rate of 0.1 mV/s during the second cycle. The voltage gaps between

https://doi.org/10.1021/acsenergylett.5c03338
ACS Energy Lett. XXXX, XXX, XXX−XXX

peaks a/c and b/d are only 54 and 17 mV for DG-VOH, compared to 146 and 59 mV for VOH. These narrower gaps indicate suppressed electrochemical polarization and improved electrochemical kinetics in DG-VOH. Figure S10 shows the CV curves of both samples at 0.1 mV/s for the initial three cycles. Compared with VOH, the highly overlapped curves of DG-VOH indicate its highly reactive reversibility. Figure 3g shows the Zn^{2+} diffusion coefficient ($D_{Zn^{2+}}$) at different voltages calculated from the galvanostatic intermittent titration technique (GITT) curves during charging and discharging. The $D_{Zn^{2+}}$ of DG-VOH ranges from $10^{-9.2}$ to $10^{-8.7}$ cm^{-2}/s during charging and it is $10^{-9.9}$−$10^{-8.6}$ cm^{-2}/s during discharging. In contrast, the $D_{Zn^{2+}}$ ranges of VOH during charging and discharging are $10^{-10.2}$−$10^{-9.3}$ cm^{-2}/s and $10^{-11.3}$−$10^{-9.2}$ cm^{-2}/s, respectively, much lower than those of DG-VOH. The faster Zn^{2+} diffusion in the lattice of DG-VOH contributes to its higher specific capacity and rate performance. Such improved Zn^{2+} diffusion kinetics of DG-VOH can be attributed to the charge shielding effect of DG molecules, which can be explained from two perspectives. First, the steric hindrance of DG molecules increases the Zn^{2+}−O distance, therefore weakening the Zn−O bond. Second, the $-NH_2$ groups of DG molecules can form coordinate bonds with Zn^{2+} ions via the empty 4*s*/4*p* orbitals of Zn, donating electrons and decreasing the positive charge of Zn^{2+}. Figure 3h shows the adsorption energy of H^+ for both samples. The lower H^+ adsorption energy of DG-VOH further verifies the charge shielding effect of DG molecules. The lower H^+ adsorption energy in DG-VOH also hinders the detrimental co-intercalation/de-intercalation of H^+ during cycling.

Figure 4a,b shows the *in situ* XRD patterns of DG-VOH and VOH for the initial three cycles, respectively. DG-VOH exhibits two distinguished lattice planes: the (001) plane ranges from 5° to 10°, and the (110) plane ranges from 24° to 27.5°. VOH shows only the (001) plane, which stands for the interlayer spacing between [VO] layers. For both samples, the interplanar spacing of the (001) plane increases during charging and decreases during discharging. As previously reported, the binding between lattice oxygen and inserted zinc ions shrinks the interlayer spacing.[14] The de-intercalation of Zn^{2+} during charging reduces the binding between [VO] layers, expanding the interlayer spacing. Similarly, the intercalation of Zn^{2+} leads to the enhanced interaction and the shrinkage of interlayer spacing. Note that for both samples, the $Zn_x(CF_3SO_3)_y(OH)_{2x-y}\cdot nH_2O$ (BZS) phase rises when discharged to lower than 0.6 V and disappears when charged above 0.8 V, which is attributed to the co-intercalation of H^+ from the electrolyte.[44] This byproduct has been proved to adhere to the surface of vanadium oxide, mask the X-ray diffraction signal, and raise the interfacial impedance.[44−46] Figure 4c shows the *in situ* pH test results of both samples during the initial two cycles, conducted under the same current density (0.1 A/g). For both samples, the pH of electrolyte rises during the discharging process and decreases during charging. This phenomenon further corroborates the co-intercalation/de-intercalation of H^+. The raise pH intensifies the dissolution of vanadium-based cathode materials.[47] The H^+ intercalation is reported to hinder the diffusion of Zn^{2+}, cause excessive lattice expansion, and lead to the formation of byproducts, such as BZS.[48] Compared with that of VOH (from 3.95 to 4.15), DG-VOH shows less pH fluctuation during cycling (from 3.95 to 4.03), indicating the preintercalation of DG molecules can inhibit H^+ intercalation, which improve the Zn^{2+} diffusion kinetics, hinder the structural stress and vanadium dissolution, and reduce the interfacial impedance. The suppressed H^+ intercalation in DG-VOH is attributed to its downshifted *d*-band center (as illustrated in Figure 2f), which results in a reduced energy overlap between the V 3*d* states and the H 1*s* orbital. This weaker hybridization reduces the formed antibonding states to lower energies, becoming more easily occupied by electrons.[49] The higher occupied antibonding states weaken the lattice-hydrogen bonds and reduce the adsorption of H^+, subsequently hindering H^+ intercalation.[50] This provides new insight into the optimization mechanism of guest species preintercalation. Figure 4d,e shows the in situ EIS test of DG-VOH during discharging and charging. The batteries were activated for a cycle at 0.5 A/g. The larger semicircle radius and the larger slope of oblique tail indicate the larger R_{ct} and slower Zn^{2+} diffusion, respectively. R_{ct} increases during discharging, which is due to the increased concentration of Zn^{2+} in the lattice during discharging hindering the subsequent Zn^{2+} intercalation and diffusion, decreasing the interfacial charge transfer and Zn^{2+} diffusion rate.[22] Similarly, R_{ct} and W_o decreased during charging because of the de-intercalation of Zn^{2+}. The characterizations of the morphology/structure of the postcycling (for 1000 cycles at 4 A/g) and pristine DG-VOH electrode are performed, respectively, as shown in Figures 4f,g andS12. Figure 4f shows the XRD patterns. The signal of the (001) plane of the cycled electrode is significantly diminished compared with that of the pristine electrode. The intercalated Zn^{2+} ions between [VO] layers cause lattice distortion and decrease the long-range order of the lattice, weakening the diffraction signal of (00*l*) planes. The (020) plane shows no obvious change in both intensity and position after cycling. This indicates the Zn^{2+} intercalation/de-intercalation completely occurs within the interlayer spacing. Figure 4g presents the XPS spectra of V $2p_{3/2}$. The cycled electrode shows a higher ratio of V^{4+} than that of the pristine electrode. This can be attributed to the lattice trapped Zn^{2+} ions, which de-intercalated no completely during the first charging, as shown in Figure 4h,[14] which are found to enhance the electrical conductivity and stabilized the [VO] layers.[16] Due to the electrical neutrality requirement, trapped Zn^{2+} leads to the reduction of V^{5+} to V^{4+}, increasing the ratio of V^{4+} and V 3*d* electron occupation. Figure S11a shows the XPS valence band. The increased intensity of the V 3*d* peak in the cycled electrode further verifies the reduction of V^{5+}. The XPS spectra of N 1*s* are shown in Figure S11b. The peak at about 400 eV mainly originates from the $-NH_2$ group, and the peak at ∼402 eV is attributed to quaternary nitrogen cations. The acid environment during hydro-thermal synthesis leads to the transition of the $-NH_2$ group to quaternary nitrogen cations. During cycling, the quaternary nitrogen cations are reduced, resulting in the disappearance of the quaternary nitrogen peak. Figure S11c shows the XPS spectra of O 1s. The ratio of oxygen vacancies/lattice oxygen for the postcycling and pristine electrode are 0.21 and 0.24, respectively, which shows no significant change, indicating the stability of oxygen vacancy content during cycling. The SEM images of DG-VOH at the cycled state and pristine states are shown in Figure S12. No obvious changes in the shape and size of DG-VOH particles occur after cycling, indicating the stable morphology of the DG-VOH cathode.

The modification mechanisms of 1,3-diaminoguanidine molecules (DG) preintercalation on hydrated vanadium pentoxide are thoroughly deciphered in this work. The

https://doi.org/10.1021/acsenergylett.5c03338
ACS Energy Lett. XXXX, XXX, XXX−XXX

introduction of DG molecules leads to the partial reduction of V^{5+} to V^{4+} via the formation of oxygen vacancies. This reduction results in distortion of the $[VO_6]$ octahedra, thereby altering the ligand field of DG-VOH and shifting the V 3*d* and the O 2*p* bands to lower energy levels. DFT calculations confirm that the modified band structure of DG-VOH enables the Fermi level across the conduction band of DG-VOH, enhancing its electronic conductivity. The preintercalation of DG molecules also shields the positive charge of Zn^{2+} and reduces the interaction between Zn^{2+} and lattice oxygen, enhancing the Zn^{2+} diffusion kinetics. More importantly, the lower energy level of V 3*d* in DG-VOH suppresses the co-insertion of H^+ during cycling and hinders the formation of byproduct $(Zn_x(CF_3SO_3)_y(OH)_{2x-y}\cdot nH_2O)$ on the surface of cathode, alleviating the lattice strain, the dissolution of vanadium, and the increase of interfacial impedance. As a result, DG-VOH achieves a specific capacity of 437.8 mAh/g and a capacity retention of 91% after 5000 cycles at 8 A/g, significantly outperforming the pristine VOH. These findings unveil the fundamental optimization mechanisms of organic molecule preintercalation, paving the way for designing high-performance cathode materials for ZIBs.

■ ASSOCIATED CONTENT

Supporting Information

The Supporting Information is available free of charge at https://pubs.acs.org/doi/10.1021/acsenergylett.5c03338.

Additional experimental methods, calculations, data, and figures, including synthesis, electrode preparations, electrochemical testing, DFT calculations, TEM images of DG-VOH, TG-DSC curves of VOH, XPS spectra of O 1s, crystal structure for PDF refinement, partial PDF curves, valence band region of XPS spectra, EIS spectra, voltage profile, CV curves, and XPS spectra and SEM images of the postcycling electrode (PDF)

■ AUTHOR INFORMATION

Corresponding Authors

Wei-Hsiang Huang − *Sustainable Electrochemical Energy Development (SEED) Center, National Taiwan University of Science and Technology, Taipei 106, Taiwan; National Synchrotron Radiation Research Center (NSRRC), Hsinchu 300092, Taiwan;* orcid.org/0000-0001-9503-0373; Email: huang.sean@nsrrc.org.tw

Chaofeng Liu − *Interdisciplinary Materials Research Center, School of Materials Science and Engineering, Tongji University, Shanghai 201804, China;* orcid.org/0000-0003-2942-1418; Email: chaofeng@tongji.edu.cnc

Guozhong Cao − *Department of Materials Science and Engineering, University of Washington, Seattle, Washington 98195, United States;* orcid.org/0000-0001-6539-0490; Email: gzcao@uw.edu

Authors

Heng Liu − *Interdisciplinary Materials Research Center, School of Materials Science and Engineering, Tongji University, Shanghai 201804, China*

Menghao Yang − *Interdisciplinary Materials Research Center, School of Materials Science and Engineering, Tongji University, Shanghai 201804, China;* orcid.org/0000-0001-7926-5113

Quan Zong − *College of Materials and Chemistry, China Jiliang University, Hangzhou, Zhejiang 310018, China;* orcid.org/0000-0001-7184-7477

Min-Hsin Yeh − *Department of Chemical Engineering, National Taiwan University of Science and Technology, Taipei 10607, Taiwan; Sustainable Electrochemical Energy Development (SEED) Center, National Taiwan University of Science and Technology, Taipei 106, Taiwan;* orcid.org/0000-0002-6150-4750

Chun-Chi Chang − *Graduate Institute of Applied Science and Technology, National Taiwan University of Science and Technology, Taipei 10607, Taiwan*

Long Yang − *Interdisciplinary Materials Research Center, School of Materials Science and Engineering, Tongji University, Shanghai 201804, China;* orcid.org/0000-0001-8731-0172

Complete contact information is available at: https://pubs.acs.org/10.1021/acsenergylett.5c03338

Notes

The authors declare no competing financial interest.

■ ACKNOWLEDGMENTS

This work is financially supported by the National Natural Science Foundation of China (52102277, 52472238, 52302193) and the Fundamental Research Funds for the Central Universities, conducted by Tongji University. The authors acknowledge the Experimental Center of Materials Science and Engineering in Tongji University. Research facilities of soft-XAS was provided by the beamline of TLS BL20A1, National Synchrotron Radiation Research Center (NSRRC) in Taiwan. The synchrotron radiation PDF experiments were performed at BL02B1 of SPring-8 with the approval of Japan Synchrotron Radiation Research Institute (JASRI, Proposal No. 2024A1878).

■ REFERENCES

(1) Wang, C.-Y.; Liu, T.; Yang, X.-G.; Ge, S.; Stanley, N. V.; Rountree, E. S.; Leng, Y.; McCarthy, B. D. Fast Charging of Energy-Dense Lithium-Ion Batteries. *Nature* **2022**, *611*, 485−490.

(2) Li, S.; Xu, X.; Wang, K.; Chen, W.; Lu, X.; Song, Z.; Hwang, J.-Y.; Kim, J.; Bai, Y.; Liu, Y.; Xiong, S. Textured $Na_2V_6O_{16}\cdot 3H_2O$ Cathode Tuned Via Crystal Engineering Endows Aqueous Zn-Ion Batteries with High Rate Capability and Adequate Lifespan. *ACS Energy Lett.* **2022**, *7*, 3770−3779.

(3) Zeng, Y.; Luan, D.; Lou, X. W. Recent Advances in Electrode Engineering Strategies for Aqueous Zn-Based Batteries. *Chem.* **2023**, *9*, 1118−1146.

(4) Jia, X.; Liu, C.; Neale, Z.; Yang, J.; Cao, G. Active Materials for Aqueous Zinc Ion Batteries: Synthesis, Crystal Structure, Morphology, and Electrochemistry. *Chem. Rev.* **2020**, *120*, 7795−7866.

(5) Hu, B.; Li, D.; Li, M.; Jiang, J.; Zhao, Y.; Du, T.; Zhou, Z.; Pu, H.; Ma, G.; Li, Z. Dual Active Sites Along with Hydrophobic Structure Modulation of Vanadium Hexacyanoferrate for Aqueous Zn-Ion Batteries. *Inorg. Chem.* **2025**, *64*, 6042−6052.

(6) Hu, B.; Li, D.; Li, M.; Jiang, J.; Zou, Y.; Deng, Y.; Zhou, Z.; Pu, H.; Ma, G.; Li, Z. Conductive Network Enhanced Self-Assembled Diphasic Prussian Blue Analogs for Aqueous Zinc-Ion Batteries. *J. Mater. Chem. C* **2025**, *13*, 6736−6744.

(7) Yan, M.; He, P.; Chen, Y.; Wang, S.; Wei, Q.; Zhao, K.; Xu, X.; An, Q.; Shuang, Y.; Shao, Y.; Mueller, K. T.; Mai, L.; Liu, J.; Yang, J. Water-Lubricated Intercalation in $V_2O_5\cdot nH_2O$ for High-Capacity and High-Rate Aqueous Rechargeable Zinc Batteries. *Adv. Mater.* **2018**, *30*, No. 1703725.

(8) Bi, X.; Yu, A.; Zhang, J.; Yu, J.; Li, C.; Ren, Y.; Lin, K.; Chai, J.; Xue, Q.; Xie, Y.; Cheng, Y.; Chang, X.; Lu, X.; Yang, L.; He, R.; Zeng, G.; Huang, C.; Qi, X.; Qi, X.; Zhang, C.; Arbiol, J.; Jacob, T.; Cabot, A. Ca^{2+}-Preintercalated V_2O_5 as a Dual-Function Cathode Additive for Polyiodide Anchoring in Zn−I_2 Batteries. *ACS Nano* **2025**, *19*, 25438−25454.
(9) Hu, B. B.; Li, D. S.; Cheng, H.; Wang, P. P.; Yang, X. Y.; Li, M. X.; Pu, H.; Ma, G. Q.; Li, C. S.; Sun, Y.; Li, Z. Organic Molecules Intercalated Hydrated Vanadium Oxide with Bifunctional of Hydrophobicity and Pillar in Aqueous Zinc-Ion Batteries. *Rare Met.* **2025**, *44*, 7209−7219.
(10) Sun, Q.; Cheng, H.; Sun, C.; Liu, Y.; Nie, W.; Zhao, K.; Lu, X.; Zhou, J. Architecting a Hydrated $Ca_{0.24}V_2O_5$ Cathode with a Facile Desolvation Interface for Superior-Performance Aqueous Zinc Ion Batteries. *ACS Appl. Mater. Interfaces* **2021**, *13*, 60035−60045.
(11) Li, J.; McColl, K.; Lu, X.; Sathasivam, S.; Dong, H.; Kang, L.; Li, Z.; Zhao, S.; Kafizas, A. G.; Wang, R.; Brett, D. J. L.; Shearing, P. R.; Corà, F.; He, G.; Carmalt, C. J.; Parkin, I. P. Multi-Scale Investigations of δ-$Ni_{0.25}V_2O_5{\cdot}nH_2O$ Cathode Materials in Aqueous Zinc-Ion Batteries. *Adv. Energy Mater.* **2020**, *10*, No. 2000058.
(12) Yang, Y.; Tang, Y.; Fang, G.; Shan, L.; Guo, J.; Zhang, W.; Wang, C.; Wang, L.; Zhou, J.; Liang, S. Li^+ Intercalated $V_2O_5{\cdot}nH_2O$ with Enlarged Layer Spacing and Fast Ion Diffusion as an Aqueous Zinc-Ion Battery Cathode. *Energy Environ. Sci.* **2018**, *11*, 3157−3162.
(13) Cheng, X.; Xiang, Z.; Yang, C.; Li, Y.; Wang, L.; Zhang, Q. Polar Organic Molecules Inserted in Vanadium Oxide with Enhanced Reaction Kinetics for Promoting Aqueous Zinc-Ion Storage. *Adv. Funct. Mater.* **2024**, *34*, No. 2311412.
(14) Liu, H.; Yang, L.; Shen, T.; Li, C.; Kang, T.; Niu, H.; Huang, W.-H.; Chang, C.-C.; Yang, M.; Cao, G.; Liu, C. Distorting Local Structures to Modulate Ligand Fields in Vanadium Oxide for High-Performance Aqueous Zinc-Ion Batteries. *ACS Nano* **2025**, *19*, 9132−9143.
(15) Wang, M.; Zhang, J.; Zhang, L.; Li, J.; Wang, W.; Yang, Z.; Zhang, L.; Wang, Y.; Chen, J.; Huang, Y.; Mitlin, D.; Li, X. Graphene-Like Vanadium Oxygen Hydrate (VOH) Nanosheets Intercalated and Exfoliated by Polyaniline (PANI) for Aqueous Zinc-Ion Batteries (ZIBs). *ACS Appl. Mater. Interfaces* **2020**, *12*, 31564−31574.
(16) Liu, C.; Neale, Z.; Zheng, J.; Jia, X.; Huang, J.; Yan, M.; Tian, M.; Wang, M.; Yang, J.; Cao, G. Expanded Hydrated Vanadate for High-Performance Aqueous Zinc-Ion Batteries. *Energy Environ. Sci.* **2019**, *12*, 2273−2285.
(17) Lv, T.; Zhu, G.; Dong, S.; Kong, Q.; Peng, Y.; Jiang, S.; Zhang, G.; Yang, Z.; Yang, S.; Dong, X.; Pang, H.; Zhang, Y. Co-Intercalation of Dual Charge Carriers in Metal-Ion-Confining Layered Vanadium Oxide Nanobelts for Aqueous Zinc-Ion Batteries. *Angew. Chem., Int. Ed.* **2023**, *62*, No. e202216089.
(18) Ma, X.; Cao, X.; Yao, M.; Shan, L.; Shi, X.; Fang, G.; Pan, A.; Lu, B.; Zhou, J.; Liang, S. Organic−Inorganic Hybrid Cathode with Dual Energy-Storage Mechanism for Ultrahigh-Rate and Ultralong-Life Aqueous Zinc-Ion Batteries. *Adv. Mater.* **2022**, *34*, No. 2105452.
(19) Liu, H.; Niu, H.; Huang, W.-H.; Shen, T.; Li, C.; Chang, C.-C.; Yang, M.; Gao, C.; Yang, L.; Zong, Q.; Pei, Y.; Cao, G.; Liu, C. Unveiling the Local Structure and the Ligand Field of Organic Cation Preintercalated Vanadate Cathode for Aqueous Zinc-Ion Batteries. *ACS Energy Lett.* **2024**, *9*, 5492−5501.
(20) Niu, H.; Liu, H.; Yang, L.; Kang, T.; Shen, T.; Jiang, B.; Huang, W. H.; Chang, C. C.; Pei, Y.; Cao, G.; Liu, C. Impacts of Distorted Local Chemical Coordination on Electrochemical Performance in Hydrated Vanadium Pentoxide. *Nat. Commun.* **2024**, *15*, 9421.
(21) Evans, H.; Post, J.; Ross, D.; Nelen, J. The Crystal Structure and Crystal Chemistry of Fernandinite and Corvusite. *Can. Mineral.* **1994**, *32*, 339−351.
(22) Grey, L. H.; Nie, H.-Y.; Biesinger, M. C. Defining the Nature of Adventitious Carbon and Improving Its Merit as a Charge Correction Reference for XPS. *Appl. Surf. Sci.* **2024**, *653*, 159319.
(23) Togonon, J. J. H.; Longo, A.; Wernert, R.; Stievano, L.; Rovezzi, M.; Chotard, J.-N.; Iadecola, A.; Croguennec, L. Probing the Structural and Electronic Heterogeneity of $LiVPO_4F$ and $KVPO_4F$ Positive Electrode Materials by Combined X-ray Absorption and Emission Spectroscopy. *Mater. Today Chem.* **2025**, *44*, No. 102541.
(24) Shvets, P.; Maksimova, K.; Goikhman, A. In Situ Xrd and Raman Study of the Phase Transition in V_2O_5 Xerogels. *J. Non-Cryst. Solids* **2024**, *625*, No. 122751.
(25) Sun, Q.; Cheng, H.; Yuan, Y.; Liu, Y.; Nie, W.; Zhao, K.; Wang, K.; Yao, W.; Lu, X.; Lu, J. Uncovering the Fundamental Role of Interlayer Water in Charge Storage for Bilayered $V_2O_5 \cdot nH_2O$ Xerogel Cathode Materials. *Adv. Energy Mater.* **2023**, *13*, No. 2202515.
(26) Wang, J.; Wang, J.; Jiang, Y.; Xiong, F.; Tan, S.; Qiao, F.; Chen, J.; An, Q.; Mai, L. $CaV_6O_{16}{\cdot}2.8H_2O$ with Ca^{2+} Pillar and Water Lubrication as a High-Rate and Long-Life Cathode Material for Ca-Ion Batteries. *Adv. Funct. Mater.* **2022**, *32*, No. 2113030.
(27) Cao, J.; Zhang, D.; Yue, Y.; Yang, X.; Yang, C.; Niu, J.; Zeng, Z.; Kidkhunthod, P.; Wannapaiboon, S.; Zhang, X.; Qin, J.; Lu, J. Unveiling the X-Ray Absorption Chemistry of $H_{3.78}V_6O_{13}$ Cathode for Aqueous Zinc-Ion Batteries. *Adv. Funct. Mater.* **2023**, *33*, No. 2307270.
(28) Farrow, C. L.; Juhas, P.; Liu, J. W.; Bryndin, D.; Božin, E. S.; Bloch, J.; Proffen, T.; Billinge, S. J. L. Pdffit2 and Pdfgui: Computer Programs for Studying Nanostructure in Crystals. *J. Phys.: Condens. Matter.* **2007**, *19*, No. 335219.
(29) Juhás, P.; Davis, T.; Farrow, C. L.; Billinge, S. J. L. Pdfgetx3: A Rapid and Highly Automatable Program for Processing Powder Diffraction Data into Total Scattering Pair Distribution Functions. *J. Appl. Crystallogr.* **2013**, *46*, 560−566.
(30) Petkov, V.; Trikalitis, P. N.; Bozin, E. S.; Billinge, S. J. L.; Vogt, T.; Kanatzidis, M. G. Structure of $V_2O_5{\cdot}nH_2O$ Xerogel Solved by the Atomic Pair Distribution Function Technique. *J. Am. Chem. Soc.* **2002**, *124*, 10157−10162.
(31) Abbate, M.; Pen, H.; Czyżyk, M. T.; Groot, F. M. F. D.; Fuggle, J. C.; Ma, Y. J.; Chen, C. T.; Sette, F.; Fujimori, A.; Ueda, Y.; Kosuge, K. Soft X-ray Absorption Spectroscopy of Vanadium Oxides. *J. Electron Spectrosc. Redat. Phenom.* **1993**, *62*, 185−195.
(32) Wang, Y.; Wei, S.; Qi, Z.-H.; Chen, S.; Zhu, K.; Ding, H.; Cao, Y.; Zhou, Q.; Wang, C.; Zhang, P.; Guo, X.; Yang, X.; Wu, X.; Song, L. Intercalant-Induced V t2g Orbital Occupation in Vanadium Oxide Cathode toward Fast-Charging Aqueous Zinc-Ion Batteries. *Proc. Natl. Acad. Sci. U. S. A.* **2023**, *120*, No. e2217208120.
(33) Wang, D.; Jiao, Y.; Shi, W.; Pu, B.; Ning, F.; Yi, J.; Ren, Y.; Yu, J.; Li, Y.; Wang, H.; Li, B.; Li, Y.; Nan, C.; Chen, L.; Shi, S. Fundamentals and Advances of Ligand Field Theory in Understanding Structure-Electrochemical Property Relationship of Intercalation-Type Electrode Materials for Rechargeable Batteries. *Prog. Mater. Sci.* **2023**, *133*, No. 101055.
(34) Jia, X.; Liu, C.; Wang, Z.; Huang, D.; Cao, G. Weakly Polarized Organic Cation-Modified Hydrated Vanadium Oxides for High-Energy Efficiency Aqueous Zinc-Ion Batteries. *Nano-Micro Letters* **2024**, *16*, 129.
(35) Li, K.; Tao, Z.; Ma, X.; Wu, J.; Wu, T.; Guo, C.; Qi, Y.; Yu, J.; Zheng, J.; Xue, J. The Application and Research Progress of d-band Center Theory in the Field of Water Electrolysis. *Int. J. Hydrogen Energy* **2025**, *132*, 183−211.
(36) Nørskov, J. K.; Abild-Pedersen, F.; Studt, F.; Bligaard, T. Density Functional Theory in Surface Chemistry and Catalysis. *Proc. Natl. Acad. Sci. U. S. A.* **2011**, *108*, 937−943.
(37) Lazanas, A. C.; Prodromidis, M. I. Electrochemical Impedance Spectroscopy-a Tutorial. *ACS Meas. Sci. Au* **2023**, *3*, 162−193.
(38) Huang, Y.; Peng, Y.; Ouyang, Q.; Feng, Q.; Wang, H.; Zheng, D.; Wang, F.; Lu, X.; Liu, Q. Boosting Zn^{2+} Intercalation in Manganese Oxides for Aqueous Zinc Ion Batteries Via Delocalizing the d-electrons Spin States of Mn Site. *Energy Storage Mater.* **2024**, *70*, No. 103476.
(39) Zong, Q.; Zhuang, Y.; Liu, C.; Kang, Q.; Wu, Y.; Zhang, J.; Wang, J.; Tao, D.; Zhang, Q.; Cao, G. Dual Effects of Metal and Organic Ions Co-Intercalation Boosting the Kinetics and Stability of Hydrated Vanadate Cathodes for Aqueous Zinc-Ion Batteries. *Adv. Energy Mater.* **2023**, *13*, No. 2301480.

https://doi.org/10.1021/acsenergylett.5c03338
ACS Energy Lett. XXXX, XXX, XXX−XXX

(40) Zong, Q.; Wang, Q.; Liu, C.; Tao, D.; Wang, J.; Zhang, J.; Du, H.; Chen, J.; Zhang, Q.; Cao, G. Potassium Ammonium Vanadate with Rich Oxygen Vacancies for Fast and Highly Stable Zn-Ion Storage. *ACS Nano* **2022**, *16*, 4588−4598.
(41) Xing, L.; Zhang, X.; Xu, N.; Hu, P.; Wang, K.; An, Q. Mechanistic Insights of Zn-Ion Storage in Synergistic Vanadium-Based Composites. *Adv. Funct. Mater.* **2024**, *34*, No. 2312773.
(42) Hu, H.; Tai, W.; Yuan, T.; Zhao, B.; Chen, Y.; Lu, C.; Ma, S.; He, T.; Cheng, H. One-Stone-for-Two-Birds Strategy to Enhance Zinc-Ion Diffusion and Stability in Vanadium Oxide Cathodes for High-Performance Aqueous Zinc-Ion Batteries. *Appl. Surf. Sci.* **2025**, *704*, No. 163465.
(43) Tang, H.; Wan, K.; Zhang, K.; Wang, A.; Wang, M.; Xie, J.; Su, P.; Dong, H.; Sun, J.; Li, Y. Realizing Dual-Mode Zinc-Ion Storage of Generic Vanadium-Based Cathodes Via Organic Molecule Intercalation. *ACS Nano* **2024**, *18*, 30896−30909.
(44) Liu, H.; Hou, X.; Fang, T.; Zhang, Q.; Gong, N.; Peng, W.; Li, Y.; Zhang, F.; Fan, X. Boosting Zinc-Ion Storage in Hydrated Vanadium Oxides Via Migration Regulation. *Energy Storage Mater.* **2023**, *55*, 279−288.
(45) Tang, B.; Shan, L.; Liang, S.; Zhou, J. Issues and Opportunities Facing Aqueous Zinc-Ion Batteries. *Energy Environ. Sci.* **2019**, *12*, 3288−3304.
(46) Liu, H.; Hou, X.; Zhang, Q.; Peng, W.; Li, Y.; Fan, X. Representative by-Products of Aqueous Zinc-Vanadium Batteries: Origins, Roles, Strategies, and Prospects. *Adv. Energy Mater.* **2025**, *15*, No. 2406171.
(47) Hu, X.; Yue, Y.; Peng, X. Release Kinetics of Vanadium from Vanadium (III, IV and V) Oxides: Effect of Ph, Temperature and Oxide Dose. *J. Environ. Sci.* **2018**, *67*, 96−103.
(48) Deng, Y.; Zhang, B.; Fan, X.; Qiu, Y.; Lin, Y.; Chen, J.; Zhang, J.; Chen, Z.; Liu, Z.; Wang, Q.; Wu, M.; Yang, C. Visualizing the H/Zn Co-Intercalation and the Zn Intercalation Mechanisms in Cathode to Boost Zinc-Ion Battery Performance. *Energy Storage Mater.* **2025**, *80*, No. 104445.
(49) Hammer, B.; Norskov, J. K. Why Gold Is the Noblest of All the Metals. *Nature* **1995**, *376*, 238−240.
(50) Nørskov, J. K. Electronic Factors in Catalysis. *Prog. Surf. Sci.* **1991**, *38*, 103−144.

https://doi.org/10.1021/acsenergylett.5c03338
ACS Energy Lett. XXXX, XXX, XXX−XXX